MIT
International Center for
Air Transportation

A PERFORMANCE COMPARISON OF ESTOL AND EVTOL AIRCRAFT

Christopher B. Courtin, Ara Mahseredjian, Annick J. Dewald, Mark Drela, R. John Hansman

This report presents research published under the same title at the 2021 American Institute of Aeronautics and Astronautics (AIAA) Aviation forum. Citations should be made to the original work

Report No. ICAT-2021-02
August 2021

MIT International Center for Air Transportation (ICAT)
Department of Aeronautics & Astronautics
Massachusetts Institute of Technology
Cambridge, MA 02139 USA

A Performance Comparison of eSTOL and eVTOL Aircraft

Christopher Courtin*, Ara Mahseredjian†, Annick Dewald‡, Mark Drela§, R. John Hansman¶
Massachusetts Institute of Technology, Cambridge, 02139, USA

Electric short takeoff and landing (eSTOL) aircraft and electric vertical takeoff and landing (eVTOL) aircraft are being developed for missions where availability of ground infrastructure is a critical design driver. Because eSTOL aircraft can generate high effective lift coefficients through the interaction of the wing, flaps, and distributed propellers they can achieve takeoff and landing distances comparable with the ground footprint proposed for eVTOL facilities. eSTOL aircraft require smaller propulsion systems and less energy for takeoff and landing than eVTOL aircraft, which in turn translates to reduced vehicle weight or increased payload, range, and/or speed.

This paper compares the performance difference between eSTOL and eVTOL aircraft, for both hybrid- and battery-electric propulsion architectures. Both tilt-duct and tilt-rotor eVTOL configurations are examined. For aircraft with an equivalent weight and span to proposed eVTOLs, eSTOL aircraft are able to carry 1.8-2.6x the payload at the same speed and range, depending on the eVTOL type and propulsion system architecture. This number is sensitive to eVTOL disk loading, design mission, and modeling of blown wing performance. The benefit of eSTOL arises primarily from reduced propulsion system weights and reduced energy consumption in the takeoff and landing phases. This benefit varies significantly with design ground footprint and payload; and less so with range and speed.

I. Nomenclature

a	Acceleration or speed of sound
A_d	Prop. disk area
AR	Aspect ratio
C_D	Drag coefficient
C_L	Lift coefficient
C_M	Pitching moment coefficient
$C_X = C_D - C_T$	Net streamwise force coefficient
ΔC_J	Jet momentum-excess coefficient
e	Span efficiency
FOM	Prop figure of merit
FF_c	Component form factor
I_{yy}	Pitch moment of inertia
L	Lift
m	Mass
$m.a.c.$	Mean aerodynamic chord
M_{CG}	Moment about center of gravity
M_{MLG}	Moment about main landing gear
M_{tip}	Tip Mach number
MTOW	Maximum takeoff weight
q	Pitch rate or dynamic pressure
Q_m	Motor torque
Q_c	Component interference factor
R	Prop Radius
s	Distance along runway
S	Wing reference area
S_{wet}	Wetted area
T/W	Thrust-to-weight ratio
T_c	Thrust coefficient
V	Freestream velocity
V_J	Jet velocity
V_h	Horizontal tail volume coefficient
V_v	Vertical tail volume coefficient
W	Weight
$X = D - T$	Net streamwise force
z	Height
α	Angle of attack
δ_F	Flap deflection
η_p	Propeller total efficiency
η_i	Propeller Froude efficiency
γ	Flight path angle
θ	Pitch angle
ω	Rotation rate
ρ	Density

*Graduate Student, Department of Aeronautics and Astronautics, AIAA Member.
†Graduate Student, Department of Aeronautics and Astronautics, AIAA Student Member.
‡Graduate Student, Department of Aeronautics and Astronautics, AIAA Student Member.
§Terry J. Kohler Professor, Department of Aeronautics and Astronautics, AIAA Fellow.
¶T. Wilson Professor, Department of Aeronautics and Astronautics, AIAA Fellow.

II. Introduction

Currently there is widespread interest in the development of aircraft for a variety of urban and regional air mobility missions, connecting major population centers to the surrounding region and addressing the existing transportation gap between short-range ground transport and long-range commercial air travel [1] [2]. One feature of many of these missions is that it is desirable to operate from areas with limited ground infrastructure, to allow direct access to cargo hubs or high population density areas outside of the traditional airport infrastructure.

eVTOL aircraft are being widely proposed for these missions, as they offer the minimum ground footprint available for aerial operations. However, the large propulsion systems needed to conduct the vertical flight phase of the mission reduce the payload and range capability of the vehicle for a given weight. A potential alternative to eVTOL aircraft for some missions are electric Short Takeoff and Landing (eSTOL) aircraft. eSTOL aircraft use the slipstream from propellers distributed along the wing leading edge to significantly enhance the vehicle effective lift coefficient. This arrangement, known as blown lift, can lead to dramatically reduced takeoff and landing distances. Recent flight testing of a subscale demonstrator [3] has shown that blown lift vehicles can generate lift coefficients greater than 10, which may enable GA-sized aircraft to have takeoff and landing ground rolls under 100ft [4]. This capability may make eSTOL aircraft a feasible option for some regional and urban air mobility applications where eVTOL aircraft are widely proposed [5] [6] [7].

The primary advantage of eSTOL aircraft is that, because the wing is used to generate lift in all phases of flight, smaller and lighter propulsion systems are required than for aircraft capable of vertical flight. This can lead to increased mission capability (payload or range) for a given weight, or reduced weight/cost for a given mission. The magnitude of this advantage will depend strongly on how short of a runway is required, as well as other parameters of the design mission.

Another significant factor is the type of propulsion system used. Currently, most eVTOL concepts being proposed are battery-electric, which reduces the noise, local emissions, and potentially cost of the aircraft but limits them to short range missions due to the poor energy density of current or near-future batteries relative to hydrocarbon fuels. Both battery-electric and hybrid-propulsion systems are being proposed for eSTOL aircraft. Apart from increased range, an additional benefit of hybrid propulsion systems for eVTOL and eSTOL aircraft is that batteries can be used to provide additional power during the high-power takeoff and landing phases of flight, allowing the turbine to be sized for maximum efficiency during cruising flight.

This paper will attempt to quantify the performance difference between eSTOL and eVTOL aircraft, and examine how that difference varies with design mission and runway lengths. This comparison will be made between aircraft with both battery- and hybrid-electric propulsion systems, with the main focus on hybrid propulsion systems.

There are many eVTOL configurations currently in development, but relatively little detailed performance data or information about the underlying technology assumptions on those designs are publicly available, and design missions also vary widely. This makes direct comparison difficult. Instead, two common eVTOL configurations, a tilt-duct and a tilt-rotor, will be modeled with the same set of physical models and mission assumptions as the eSTOL vehicle in order to try and make as fair a comparison as possible.

Due to the large number of parameters that go into this type of broad modeling effort, the results are sensitive to a number of assumptions about the aircraft. Those with the highest sensitivities are identified and areas where improved modeling is needed in future efforts are highlighted. There is uncertainty in modeling some of the important details of both eSTOL and eVTOL performance, as discussed below. The results here are not meant to be indicative of any specific vehicles but rather are meant to show the key trends in relative performance between configurations.

Section III gives a brief overview of eSTOL aircraft. Section IV describes the approach taken to modeling eSTOL and eVTOL aircraft and how key drivers of the designs are captured. Section V shows some comparisons to published data which validate this model. Section VI shows the comparison between battery-electric eSTOL and eVTOL aircraft, battery-electric and hybrid-electric eSTOL aircraft, and hybrid-electric eSTOL and eVTOL aircraft.

III. eSTOL Overview

The lift augmentation of a blown wing, shown in cross-section in Figure 1,arises from the deflection of the propeller wake by the trailing edge flaps of the wing. The magnitude of this augmentation is a function of the strength of the jet relative to the freestream, as well as the wing angle of attack α and the jet deflection δ_j.

It can be shown [8] [9] [4] that the key parameter which quantifies the relative strength of the blowing is the jet

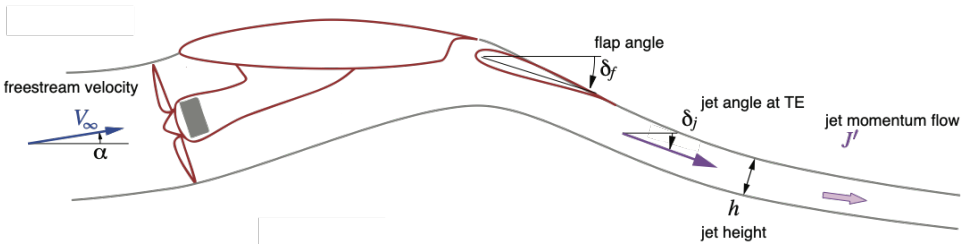

Fig. 1 The lift augmentation of a blown wing is proportional to the jet momentum J', the angle of attack α, the freestream velocity V_∞, and the jet deflection angle δ_j

momentum-excess coefficient ΔC_J.

$$\Delta C_J = \frac{A_d}{S}\left(\frac{V_J^2}{V^2} - 1\right)\left(\frac{V}{V_J} + 1\right) \tag{1}$$

This term is analogous to the more common coefficient T_c; when the jet velocity is large relative to the freestream, the two are equivalent.

$$T_c = \frac{T}{qS} = \frac{\Delta C_J}{\frac{V}{V_J} + 1} \tag{2}$$

From either equation, it can be seen that the value of ΔC_J will vary with both changing thrust levels and changing freestream velocity.

This coupling between C_L, T, and V presents a complication when using conventional methods to estimate the takeoff ground roll of an eSTOL aircraft, which are typically based on an *a priori* value of $C_{L_{max}}$. For a blown lift aircraft $C_{L_{max}}$ will depend strongly on the installed power. C_L (and the associated drag) will also vary continuously along the takeoff and landing ground roll.

In order to estimate the takeoff and landing distances for this paper, a model of $C_L(\alpha, \delta_F, \Delta C_J; \text{geom.})$, $C_X(\alpha, \delta_F, \Delta C_J; \text{geom.})$, and $C_m(\alpha, \delta_F, \Delta C_J; \text{geom.})$ was constructed based on existing wind tunnel data. The equations of motion for the takeoff and landing ground roll were integrated to estimate the takeoff and landing distances, with the forces at each point estimated based on the instantaneous airspeed, angle of attack, as well as the installed power. This provides an unambiguous coupling between the takeoff performance of the vehicle and the size of the propulsion system, and also allows the inclusion of additional factors which may limit the takeoff distance, such as the ability of the tail to rotate the aircraft at low speeds. Appendix A provides more details about this approach.

Because blowing also suppresses boundary layer separation and increases the stall angle of the wing [10], the maximum angle of attack (and hence $C_{L_{max}}$) may be quite large. However, the magnitude of this effect and how it changes with different levels of blowing is difficult to predict. Additionally, because effective blowing varies with speed for fixed power, it is not clear that defining takeoff speed or landing speed by a fixed C_L margin from $C_{L_{max}}$ is appropriate as the aircraft may be close to the stall angle of attack even with a large margin to $C_{L_{\max}}$.

What is required is an adequate margin of safety to the stall angle on takeoff and landing. For this work, the safety margin was defined by a maximum allowable angle of attack of 10° at the moment of liftoff. 10° was chosen to be at least 10° below the stall angles for representative takeoff configurations shown in [10]. Previous airworthiness studies on blown lift aircraft [11] suggest this may provide an adequate margin of safety, but further work to define this for eSTOL aircraft is required. Other factors (such as control authority or stability) may limit the maximum C_L that is possible. Those constraints are not considered here. For the remainder of this paper, takeoff and landing C_L quoted will be touchdown and liftoff C_L, at an angle of attack of <= 10°.

IV. Analysis Approach

The approach taken to conduct this analysis was to formulate the sizing of eSTOL and eVTOL aircraft as an optimization problem, in order to make appropriate selections of vehicle design parameters (such as installed power, wing loading, etc) for a wide range of specified design missions and ensure that the comparison is not biased by poor arbitrary choices. This is especially true for eSTOL aircraft, where C_L is strongly dependent on power and the best balance of increased lift augmentation/installed power and decreased wing loading to achieve short takeoff distances is not obvious.

The high-level approach to this comparison is shown in Figure 2. A common library of aircraft component models was developed, which feed into separate eVTOL and eSTOL vehicle optimization frameworks. These different frameworks account for the physics unique to the different aircraft (blown lift for eSTOL vehicles, vertical flight for eVTOL vehicles). The same design mission inputs (payload, range, maximum speed, etc.) are then specified for both frameworks. Typically, MTOW is the optimization objective function and basis of comparison, but other objectives (such as payload or range for a specified weight) are also used.

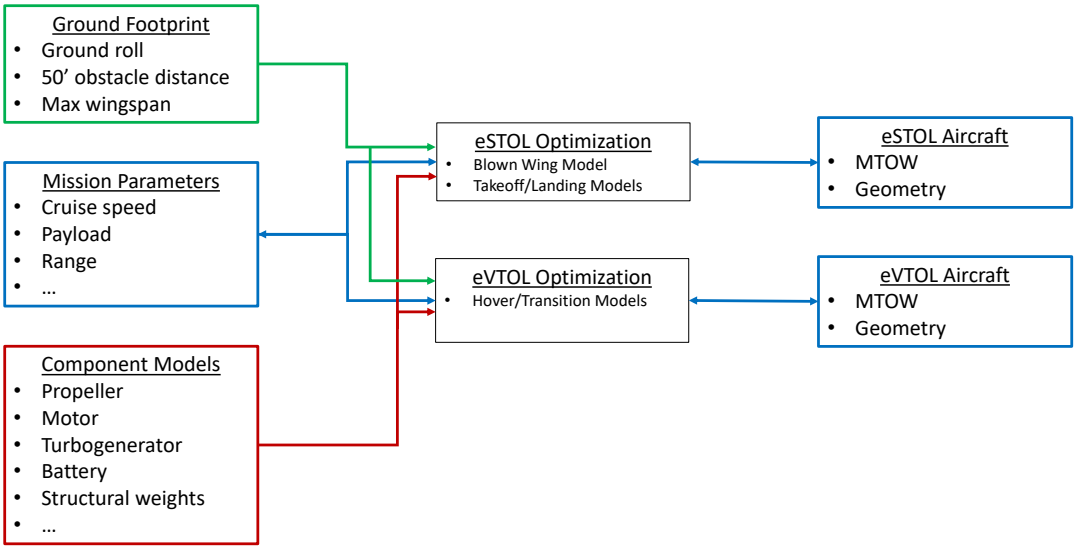

Fig. 2 Analysis overview for comparing eSTOL and eVTOL aircraft with comparable ground footprints, mission parameters, and component models.

In order to efficiently solve these problems, they were formulated as non-linear programs using Aerosandbox [12], which is an automatically differentiable Python framework for aircraft design optimization. Typical solution times for the problems in this paper were on the order of 1-30 secs per design point, depending on the number of design variables (typically hundreds to a few thousand) and problem formulation. Aerosandbox is built on the CasADi [13] package and the interior-point solver IPOPT [14].

A. Vehicle Architectures

There are a wide variety of eVTOL aircraft architectures being developed by many different manufacturers and a thorough comparison between them is beyond the scope of this paper. For comparison with the eSTOL aircraft, two representative configurations were chosen, a tilt-duct and tilt-rotor aircraft. Sketches of these configurations are shown in Figure 3.

For the purposes of this study, there is an imposed relationship between rotor diameter and wing span. On the eSTOL aircraft, all propellers must fit along the span of the wing, with 5% propeller diameter spacing between rotors. The eSTOL aircraft analyzed here has eight propellers.

For the tilt-duct eVTOL, the number of rotors is fixed at 36, with 24 on the wing and 12 on the canard. The total fraction of the wing semi-span covered by the rotors is fixed at 57%, based on the published wingspan of 13.9m, fuselage width of 1.7m, and fan diameter of 0.295m of a tilt-duct vehicle [15].

For the tilt-rotor eVTOL, six tilting rotors are assumed. Each rotor diameter is assumed to be half the semi-span. In order to provide adequate spacing between the rotors, the outboard two rotors are placed at the wing tips. For this configuration, the span comparable to an eSTOL or tilt-duct configuration is taken to be the rotor tip-to-tip length.

In all three cases, the disk loading of the aircraft is tied to the span of the wing. As will be seen, the assumed disk loading has a significant impact on the required power and associated propulsion system weight.

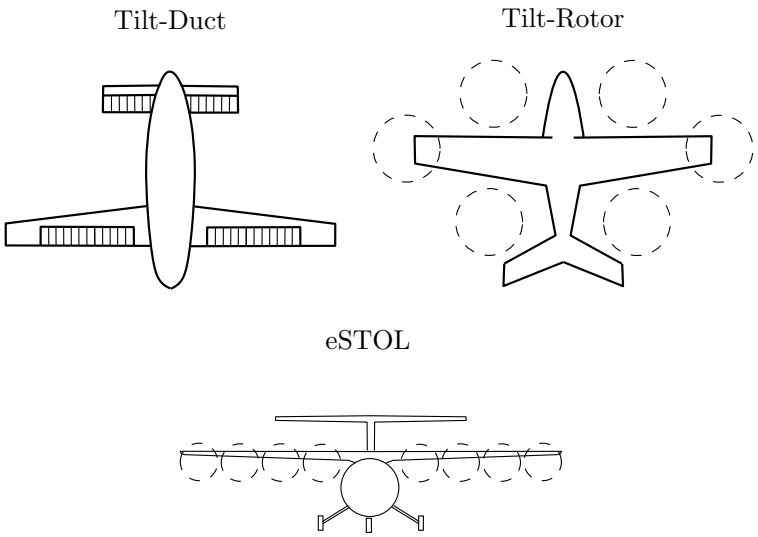

Fig. 3 Architectures of the eSTOL and eVTOL aircraft analyzed

Empennage sizing is based on fixed tail volumes. $V_v = 0.1$ and $V_h = 1.0$ are used for the eSTOL configuration. The specified tail volume is an estimated minimum for low-speed maneuvering and trim capability. The tail may also be sized by takeoff rotation, as discussed in Appendix A. No vertical tail is assumed on either the tilt-duct or tilt-rotor configurations. To account for the larger v-tail in the tilt-rotor configuration, the tail volume used ($V_h = 0.8$) is twice that of the tilt-duct ($V_h = 0.4$).

Motor Sizing Cases For the eVTOL configurations, the motors were sized for a 100 ft/min climb capability with two motors out. In the event of a single motor failure, power must be reduced to an opposing motor in order to keep the thrust symmetric [16]. This has a more significant impact on the tilt-rotor than tilt-duct configurations due to the lower motor count. For the eSTOL aircraft, since the full-power flight time is so short (<10 sec on takeoff) it is assumed that the surge capability of the motors could compensate for a single motor failure on takeoff and/or that margin is added to the runway to account for the motor out case.

No additional torque or power capability is assumed for flight control. It is assumed that this momentary power increase comes from the short-duration burst power capability of electric motors. Tip Mach number constraints during normal hover may also size the motors, as low noise is an important consideration. A 0.45 tip Mach in hover or at takeoff is assumed for all vehicles, based on the design targets cited in [15]. The relationship between tip Mach and the max RPM is estimated from

$$M_{tip} = \sqrt{V^2 + (\omega R)^2}/a \tag{3}$$

The required motor torque can then be estimated from $Q_m = P_{req}/\omega$, and the motor weight estimated based on a specific torque. As will be discussed in Section IV.C, motor weight is also estimated based on specific power required for the engine-out conditions, and either constraint may size the motor. That assumes that increased tip Mach may be acceptable in an engine-out scenario. For the tilt-duct aircraft, noise considerations drive the design of the ducted fan and so any sizing for motor torque was not included for that configuration.

B. Mission Performance

For sizing the various vehicles, the design mission was broken up into five segments; takeoff, climb to altitude, cruise, landing, and reserve. The total range specified is the sum of the climb and cruise distance. No descent segment was modeled. The cruise altitude of the aircraft was a free parameter in the optimization, with maximum (10,000ft) and minimum (5,000 ft) altitudes specified. During the climb segment, an average rate of climb of at least 1000 ft/min was imposed. For hybrid-electric aircraft, fuel burn was calculated from the Breguet range equation. L/D, total powertrain efficiency, and specific fuel consumption for each segment were estimated based on the average segment weight, and for the climb segment at half the cruise altitude. For electric aircraft, the electric range equation was used [17] with L/D and efficiency calculated in the same way.

1. eVTOL Takeoff and Landing

The tilt-duct eVTOL aircraft takeoff and landing performance models were based on the ducted fan performance models proposed in [15]. Motor shaft power in hover $P_{m,h}$ is given by

$$P_{m,h} = \frac{\frac{1}{2}\frac{T_h^{3/2}}{\sqrt{\rho_h n A_{j,h}}}}{\eta_{F,h}\eta_{D,h}} \tag{4}$$

where T_h is thrust, ρ_h is atmospheric density, n is number of ducted fans, $A_{j,h}$ is the jet area of a single ducted fan, $\eta_{F,h} = 0.88$ is fan efficiency and $\eta_{D,h} = 0.96$ is duct efficiency. During hover, $A_{j,h} = \sigma A_d$, where A_d is the disk area of the fan and $\sigma = 1.3$ [15].

For the tilt-rotor, the equation for an unducted rotor is used

$$P_{m,h} = \frac{T^{3/2}}{\sqrt{2\rho n A_d}}\frac{1}{\text{FOM}} \tag{5}$$

where the FOM = 0.64 was estimated from the data in [16]. Transition power for both configurations was modeled by

$$P_{tr,avg} = \frac{P_h + P_{tr,eff}}{2} \tag{6}$$

where

$$P_{tr,eff} = \frac{P_h}{\kappa} \tag{7}$$

where $\kappa = 10$ was assumed to be constant [15].

The power required for a vertical climb is estimated by

$$P_i = \frac{TV_v}{2}\left(1 + \left(1 - \frac{2T}{\rho A_d V_v^2}\right)^{1/2}\right) \tag{8}$$

from [18] where V_v is the vertical speed. For the ducted fan, a 23% reduction in power was estimated based on the same source, and the effective jet area was used.

Times for each flight segment are used to determine energy requirements. Takeoff hover and landing hover time assumptions are the same as those used in [15] and are given in Table 1. Takeoff and landing transition times were calculated based on a constant 0.2g acceleration from hover to $1.2V_{stall}$ in airplane mode. This acceleration matches the transition power estimate. For the eVTOL configurations the stall speed was based on a $C_{L_{\max}} = 2.5$.

Flight Segment	Flight Time [s]
Takeoff Hover	15
Landing Hover	45

Table 1 Takeoff and Landing Hover Times

2. eSTOL Takeoff and Landing

The details of the eSTOL takeoff and landing calculation approach are described in Appendix A. One important point to clarify is the way that takeoff and landing distances are specified. Takeoff distances quoted here are for the sea level, all engines operating case. Either the ground roll (brake release to liftoff) or total distance over a 50 ft obstacle are specified. Depending on the mission type, either one or the other may be the critical parameter. For example, in operations off barges, piers, or rooftops, the ground roll and not total obstacle clearance distance will define the ground footprint. In confined areas on the ground, total distance over a 50 ft obstacle may be the more critical parameter.

For initial comparisons, a takeoff ground roll of 150 ft and a landing ground roll of 100 ft are used. This is based on expected operations from a 300 ft runway (with some additional margin for obstacle clearance distance if required). The takeoff ground roll is longer due to the fact that there is some additional margin on landing for uncertainty in the touchdown point. The sensitivity to changing these assumptions is shown in Section VI.C.

On landing, only the ground roll is specified. The total distance over a 50 ft obstacle depends strongly on the achievable approach angle, which is dependent on the amount of blowing required to achieve the target lift coefficient while descending. Estimating this angle depends significantly on the details of how the blowing is distributed on the wing, the maximum flap deflection achievable, and the details of the flare maneuver. Estimating that accurately is beyond the scope of this paper, since it is not expected to size the propulsion system. However, achievable approach angle is an important consideration for some eSTOL missions and design criteria. [10] shows that approach angles steeper than the standard helicopter 8° are achievable.

C. Propulsion System Models

Figure 4 shows the propulsion system architecture modeled for both eSTOL and eVTOL configurations. For the battery-electric configurations, the elements shown within the dashed box, which comprise the turbogenerator, are omitted. Otherwise, the same component models are used in all cases. Each component is modeled based on a fixed specific power and density. These were chosen to be roughly representative of what is currently commercially available or may be in the near future.

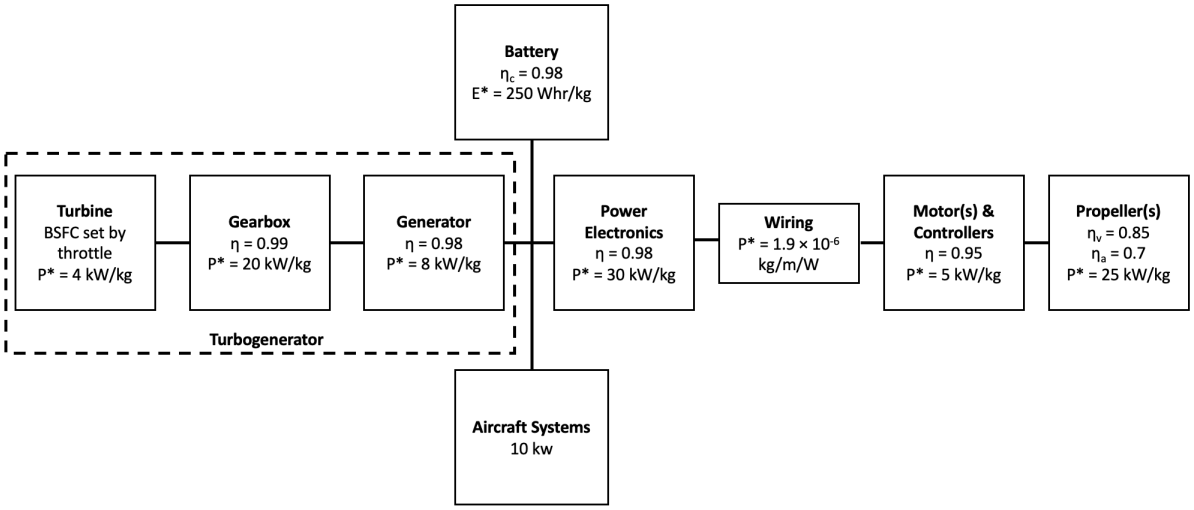

Fig. 4 Propulsion system component diagram with specific power and efficiency values

250 Wh/kg was chosen as the total battery energy density (including cell energy density, packing factor, containment, etc) based on [15]. A 25C maximum discharge rate was also specified. It should be noted that the specific energy typically sizes the battery in the all-electric case, and discharge rate in the hybrid-electric case. Battery technology is rapidly evolving and these numbers are intended to be representative of the current- or near-future state of the art.

For the hybrid configurations, an important parameter is the degree of hybridization $P_{battery}/P_{total}$; the fraction of power supplied by the battery compared to the turbine. In this model, the degree of hybridization was a free parameter in the takeoff, landing, and climb segments. It was fixed to be zero during cruise (and was one in all phases for the battery-electric configurations). The hybridization parameter allows batteries to be used to keep the turbine at its most efficient operating point during cruise. The trade between battery weight and turbine fuel efficiency depends on how the turbine BSFC varies with throttle setting. For this study, a turbine BSFC vs throttle curve from [19] was used, normalized by the BSFC at 100% throttle. This curve is for a high altitude turboprop aircraft, and may differ from modern turbogenerator variations with throttle at low altitude. Peak BSFC (at 100% throttle) is an input to the model and 0.6 lbs/hp-hr was used for hybrid eSTOL and eVTOL configurations.

In the hybrid configurations, the requirement was imposed that the battery be able to compensate for a turbine failure during either the takeoff or landing phases without loss of power. This peak power requirement at 25C discharge rate is typically the battery sizing case. Specifying a 25C discharge rate also implies an emergency full-power flight time of 2.4 minutes. For battery-only aircraft, a maximum of 80% of total battery capacity was considered usable. A battery discharge efficiency of 80% in takeoff and hover and 98% in climb and cruise was assumed for eSTOL and eVTOL hybrid and all-electric configurations. There is also a 13 kW/kg battery thermal management system that scales with peak power from the battery, based on a COTS battery cooling system.

The most important component in the propulsion system is the electric motors. Estimates for motor weight, diameter, specific power, specific torque, and efficiency are based on COTS motor specifications [20]. Specific power is assumed to be constant across a range of motor powers and sizes. In reality, motor weight is better scaled by torque requirements; this would be an important addition for future work on this comparison. Motor diameter D_{motor} was estimated from maximum power for the tilt-rotor and eSTOL configurations by the fit

$$D_{motor} = 2.32 {P_{max}}^{0.374} \tag{9}$$

where P_{max} is in kW and D_{motor} is in inches. For ducted fans, these relatively large-diameter motors may not be appropriate, and so the hub-to-fan diameter ratio published in [15] was used instead independent of power.

Propeller efficiency was estimated from

$$\eta_p = \eta_i \eta_v \tag{10}$$

where η_p is the total propeller efficiency, η_i is the ideal efficiency, and η_v represents viscous losses. $\eta_v = 0.85$ was used for eSTOL and tilt-rotor configurations during cruise. $\eta_v = 0.76$ was used for the ducted fan configuration, to approximately match the cruise efficiency based on a fan efficiency of 0.83 and a duct efficiency of 0.92 [15]. Froude efficiency η_i is estimated from the modified actuator disk relationship

$$\eta_i = \frac{2}{2 + (\sqrt{1 + T_c} - 1)/\eta_a} \tag{11}$$

where $\eta_a = 0.7$ accounts for swirl losses in the propeller wake and T_c is the propeller thrust coefficient $T/(qA_d)$. Propeller weights are scaled with power, based on propellers in a typical eSTOL size class. In reality, propeller weights will scale with both power and size; this approach may over-predict weights for the ducted fan and under-predict weights for the tilt-rotor.

No weight is included for any tilting actuators or variable-pitch propeller control mechanisms.

D. Airframe Components

Handbook methods were used to estimate the aircraft structural weights. Horizontal tail, vertical tail, fuel system, flight controls, and air conditioning system weights were all based on Raymer estimates for general aviation aircraft [21]. Wing and fuselage weights were estimated from Torrenbeek [22]. Fuselage wetted area was estimated based on an elliptical body with specified maximum cross-sectional area and fixed length. Weight reduction factors of 0.87 for the wing and tails, and 0.90 for the fuselage, were used to estimate the impacts of composite construction. 400 lbs of fixed weight were included for avionics, insulation, low-voltage electronics, fire protection, lights, and other miscellaneous systems. 40 lbs/person (passengers and pilot) was used to estimate furnishing weights. Landing gear weight was a constant 3.5% MTOW, representative of fixed gear. Retractable gear was not examined. A contingency weight factor of 5% of empty weight is also included. In the weight estimates shown below, batteries are not included in the empty weight estimates. The empty weight estimate includes the structural weights of the main airframe elements (wing, fuselage, empennage), the landing gear weight, systems and furnishings weights, and propulsion weights.

E. Drag Estimates

For eVTOL aircraft and eSTOL aircraft in the conventional flight envelope, a simple parabolic drag estimate was used.

$$C_D = C_{D_0} + \frac{C_L^2}{\pi e AR} \tag{12}$$

Zero-lift drag C_{D0} was estimated based on a drag area build-up based on wetted surface areas as described in Raymer [21] with additional components representing the drag of the landing gear and the turbine inlets for hybrid aircraft. A contingency drag of 10% is also included, which accounts for interference between the various components and other miscellaneous drag sources.

$$C_{D_0} = \frac{\sum_c C_f F F_c Q_c S_{wet_c}}{S} + C_{D_{LG}} + C_{D_{margin}} \tag{13}$$

The subscript $_c$ indicates the sum over all of the major aircraft components - the wing, horizontal and vertical tails, fuselage, pylons, and inlets. $Q_c = 1$ was used for the wing, fuselage, and pylons. $Q_c = 1.08$ was used for vertical and horizontal tails/canards. A 15% excrescence drag factor was also added to the wing, and 8% to the fuselage.

Pylon wetted area is based on the motor diameter and an assumed pylon length, which for the eSTOL aircraft is half the wing chord and for the tilt-rotor eVTOL is half the rotor radius.

For the tilt-duct configuration, there is no pylon drag included. Instead, the drag of the fan nacelles is estimated based on the Eqns. 22 and 23 in [15], using the duct length to fan diameter ratio of 2.4 published there.

For hybrid configurations, inlet drag is estimated based on an assumed 50:1 air-to-fuel mass flow ratio for the turbine at cruise to size the inlet area, with an additional 15% area for cooling air. Based on Figure 13.9 in [21], $\frac{D/q}{A_{inlet}} = 0.05$ was used as a conservative value.

V. Model Validation

A. Weight Models

Fig. 5 The Pilatus PC-6 Turbo Porter [23]

Design Variable	PC-6 Published Value
Takeoff distance over 50 ft obstacle	1,444 ft
Landing distance over 50 ft obstacle	1,033 ft
Cruise speed	115 kts
Cruise altitude	10,000 ft
Maximum payload	2,646 lbs
Payload with full fuel	2,381 lbs
Max Range at 10,000ft	500 nmi

Table 2 PC-6 Mission Specifications

To validate the underlying propulsion system and weight models against an existing aircraft, a representative aircraft mission was modelled and compared against a known vehicle. The Pilatus PC-6, pictured in Figure 5, was selected given its STOL capabilities. This aircraft is a single-engine STOL aircraft, designed to carry up to ten passengers (1130 kg payload) for a range of 500 nautical miles [24]. The key specifications of the Pilatus PC-6 Turbo Porter are enumerated in Table 2. The PC-6 is modeled with single turboprop driven propeller and no hybrid components for the comparison to the as-built PC-6 configuration. The takeoff and landing distances, as well as the cruise speed, range and

Design Variable	Modeled	Published
Maximum gross takeoff weight	6,245 lbs	6,173 lbs
Operating empty weight	2,793 lbs	2,756 lbs
Fuel weight	891 lbs	1,036 lbs
Payload weight	2,381 lbs	2,381 lbs
Wingspan	43.7 ft	52.1 ft
Wing area	303.0 ft^2	324.5 ft^2
Horizontal tail area	79.8 ft^2	82.8 ft^2
Horizontal tail volume	0.66	0.66
Vertical tail area	23.2 ft^2	25.8 ft^2
Vertical tail volume	0.03	0.03
Cruise airspeed	115 kts	115 kts
Takeoff distance over 50 ft obstacle	1444.00 ft	1444.00 ft
Landing distance over 50 ft obstacle	1033.00 ft	1033.00 ft
Range	500 nmi	500 nmi

Table 3 Comparison between published and modeled results for the PC-6

payload from Table 2 are all matched. The following table outlines the key sizing parameters against the published vehicle weights and geometries (Table 3). This includes an empty weight margin of 5% and a drag margin of 10%. These numbers are used going forward. Peak turbine power specific fuel consumption used here was 0.75 lb/hp-hr. The horizontal and vertical tail volumes were fixed a priori to match those of the Pilatus PC-6.

This comparison shows generally good agreement between the PC-6 and the models being used, although the wingspan of the optimized vehicle is slightly smaller. One thing to point out is that the PC-6 is a lightweight aircraft with an empty weight fraction of about 0.45. In the subsequent analysis, the structural weights are reduced further by the composite construction weight factors applied. These may be optimistic structural weight fractions, but should not unfairly bias the comparison.

B. eVTOL Performance Models

This section compares the eVTOL performance models to published numbers available for the different configurations. Table 4 shows a comparison between published and modeled numbers for the 7-seat tilt-duct described in [15]. Takeoff weight, span, and payload are fixed inputs to the sizing model, matched to the published numbers. Maximum range was the sizing objective function. Range shown here is total range, with no reserves. In reality, some reserve mission will be required.

Generally good agreement is observed between the cruise L/D and hover power estimates. The differences arise from differences in the component efficiencies and drag buildups used (for example, a fixed landing gear is modeled).

Tilt-Duct	**Published**	**Modeled**
MTOW	7000 lb	7000 lb
Span	45.6 ft	45.6 ft
Cruise Speed	162 kts (300 km/hr)	162 kts (300 km/hr)
Payload	1360 lb (700 kg)	1360 lb (700 kg)
Total Range	98 nmi (181 km)	56 nmi (104 km)
Installed Motor Power	-	2354 kW
Hover Power, Batt.	2570 kW	2511 kW
Motor Weight	-	1109 lb
Cruise L/D	18.26	17.25
Cruise C_L	1.0	1.0
OEW	3360 lb	4052 lb
Battery	2800 lb	1589 lb
Battery specific energy	250 Wh/kg	250 Wh/kg

Table 4 Comparison of published and modeled values for a tilt-duct eVTOL. MTOW, span, and payload are fixed inputs to both models. '-' indicates no published value.

The larger differences are in the empty and battery weight estimates, and consequently the achievable range. This is due to the underlying weight models - the published aircraft has the empty weight fraction fixed at 0.48, reflecting different structural and powertrain weight models than are used in this paper.

Table 5 shows the same comparison for a tilt-rotor aircraft based on representative data in [16]. One source of uncertainty when modeling this aircraft is the appropriate rotor figures of merit and vehicle wing loading. The rotor figure of merit for the modeled rotors in hover was chosen to be 0.64 in order to match the motor shaft power values in [25] for the same rotor diameter.

With larger propellers, maximum speed during transition may be a significant factor in determining wing loading. Analysis of this in detail is beyond the scope of this paper, but an initial estimate of this consideration can be made by specifying a maximum cruise C_L=0.56. This is the design cruise C_L used on the tilt-rotor described in [25], which may reflect wing sizing for transition. It should be emphasized that in the comparisons which follow, the tilt-duct and tilt-rotor vehicles are not the aircraft being designed by any specific manufacturer respectively but rubber aircraft scaled to match different design missions and assumptions about levels of underlying technology, in order to make a comparison with eSTOL on an equal basis.

Tilt-Rotor	Published	Modeled
MTOW	4000 lb	4000 lb
Span (not including rotors)	-	43 ft
Rotor diameter	9.5 ft	9.5 ft
Cruise Speed	175 kts (200 mph)	175 kts (200 mph)
Payload	840 lb	840 lb
Total Range	157 nmi (181 mi)	74 nmi (85 mi)
Installed Motor Power	-	792 kW
Hover Power, Shaft.	418 kW	420 kW
Motor Weight	-	350 lb
Cruise L/D	-	13.6
Cruise C_L	0.56	0.56
OEW	-	2103 lb
Battery	-	877 lb
Battery specific energy	-	250 Wh/kg

Table 5 Comparison of published and modeled values for a tilt-rotor eVTOL. MTOW, span, and payload are fixed inputs to both models. '-' indicates no published value.

VI. Configuration Comparisons

The following section compares the two eVTOL configurations described above to an eSTOL aircraft with the same design mission. The configurations will be compared at a single design mission for both electric and hybrid powertrains. For the hybrid powertrain comparison, the impact of changing the parameters of the design mission (payload, range, speed) will also be shown.

A. All-electric eVTOL to All-electric eSTOL

The mission parameters for the all-electric comparison mission are shown below. One way to compare the capability of these aircraft is on the basis of maximum payload that can be carried for a fixed MTOW. 6000lbs was chosen as as a representative target MTOW. Speeds and design ranges are chosen to be comparable to the vehicles above. The maximum span, the larger of either wing span or rotor tip-to-tip diameter, is 46 ft based on the published tilt-duct span [15]. As mentioned, for all-electric aircraft, total range with no reserves is shown.

MTOW	6000 lb
Max. Span (Wing + Rotors)	46 ft
Cruise Speed	150 kts
Total Range	75 nmi
Battery specific energy	250 Wh/kg
Fuselage length	30 ft
Fuselage width	6 ft
Crew	180 lb

Table 6 Comparison mission for all-electric powertrain

Table 6 summarizes the parameters of this mission. In this comparison, single pilot operations are assumed. The weight of the pilot is not included in the payload value. For the eSTOL aircraft, a takeoff ground roll of 150ft and landing ground roll of 100ft were imposed. See Section VI.C for an assessment of the impact of changing eSTOL runway length.

Table 7 shows the results of this comparison. From this it can be seen that, for an equivalent MTOW, an eSTOL aircraft can carry approximately 1.9-2.2x the payload, depending on the eVTOL configuration being compared. This benefit arises primarily from a reduction in installed propulsion system weight.

	Tilt-Duct eVTOL	Tilt-Rotor eVTOL	eSTOL
Payload (lb)	**668**	**784**	**1474**
Empty Weights (lb)	3596	3356	2754
Battery (lb)	1556	1680	1592
Installed Motor Power (kW)	1,887	1769	672
Shaft Power, Hover (kW)	1,469	954	N/A
Total Prop. Disk Area (sq. ft)	25.8	289.3	114.2
W/S (lbs/sq.ft)	65.5	36.7	25.0
Cruise L/D	16.6	11.1	10.5

Table 7 Key parameters from comparison of battery-only eVTOL and eSTOL aircraft with a constant 6000 lb MTOW, 75 nmi range, and 150 kts cruise speed. See Table 10 for additional outputs. Payload not inclusive of 180 lb pilot.

There are several notable results of this comparison. One which is that the eSTOL configuration has a slightly lower L/D than either of the eVTOL configurations, at least for the configurations considered. This is due to the fact that there is a strong trade on wing loading for the eSTOL aircraft. Short takeoff and landing distances favor lower wing loading (all else being equal), but low wing loading reduces the cruise efficiency because of the low cruise C_L. This can be compensated for by increasing lift augmentation, but at the cost of increased propulsion system weight. The best wing- and power-loading for an eSTOL aircraft comes from finding a balance between high cruise L/D and low required takeoff power. For the eVTOL aircraft, this tension is not present and their wings can be better optimized for cruising flight. The improved L/D in cruise partially offsets the high energy consumption during takeoff and landing.

In reality, there may be significant propulsion-wing interactions in all configurations which also impact the cruise drag which are not modeled. Additionally, this calculation is sensitive to the amount of time assumed to be spent in hover relative to the cruise time - as missions get shorter or the hover time becomes longer, the benefit of eSTOL will increase.

The trade between improved cruise L/D and low takeoff/landing power consumption is also noticeable to a lesser extent between the two eVTOL configurations. The tilt-duct has a high energy consumption in the takeoff and landing phase, but improved cruise L/D means it uses less energy over the course of the mission. In terms of net payload capability, the lighter propulsion system of the tilt-rotor has a slight benefit.

The magnitude of the difference in takeoff and landing energy consumption can be seen from the difference in hover power requirements between the two configurations. This arises mainly from the different disk loading, which are much higher for the tilt-duct configuration.

One disadvantage of all-electric propulsion is that the achievable energy densities of current or near-future batteries limit its application to relatively short-range missions. All-electric aircraft are suitable for short range air taxi missions but for longer range RAM missions (150 nmi+) battery-only eVTOL, and to a lesser extent eSTOL aircraft will not be feasible, especially with current reserve mission requirements. This motivates the use of hybrid-electric propulsion systems, which combine the benefits of distributed electric propulsion with the useful range capability of conventional fuel systems.

B. All-electric eSTOL to Hybrid eSTOL

To show the performance benefits of hybrid propulsion, a hybrid-electric eSTOL and all-electric eSTOL are compared for the same mission as above. This comparison is shown in Table 8. Two variants of the hybrid eSTOL are shown. The first is the maximum payload that could be carried over the 75 nmi design mission, if a hybrid propulsion system was used instead of batteries. This is a fair comparison of the performance benefits but doesn't take advantage of the main benefit of hybrid propulsion, which is longer ranges. The second shows the maximum range that could be achieved, carrying the equivalent payload. This shows that, all else being equal, hybridization can offer a significant payload (1.6x) or range (10x) increase over an equivalent all-electric aircraft. The growth in empty weight from battery to hybrid is due to the way weights are bookkept; the battery is not included in the empty weight buildup but as its own component, and so the increase in empty weight is due to the additional turbogenerator weight even though the total weight of energy storage decreases.

Of course, hybrid powertrains do not have the benefits of zero local emissions and reduced engine noise that

	All-Electric eSTOL	Hybrid eSTOL, Max. Payload	Hybrid eSTOL, Max. Range
Payload (lb)	**1474**	**2424**	1474
Total Range (nmi)	75	**75**	**747**
Empty Weights (lb)	2754	3073	3149
Fuel (lb)	0	97	963
Battery (lb)	1592	225	234
Propulsion (lb)	647	844	856
Battery Energy (kW-hrs)	181	26	27
$f_{batt,TO}$	1.0	0.60	0.63
$f_{batt,LND}$	1.0	0.32	0.32
$f_{batt,climb}$	1.0	0.22	0.25

Table 8 Comparison of battery-only eSTOL and hybrid eSTOL aircraft with a constant 6000 lb MTOW and 150 kts cruise speed. See Table 11 for additional outputs. Payload not inclusive of 180 lb pilot.

all-electric aircraft offer. But for missions where small ground footprints and long ranges are required, they are the most practical option. Hybrid propulsion systems can be used on both eSTOL or eVTOL configurations.The comparison between hybrid eSTOL and eVTOL is shown in the following section.

C. Hybrid eSTOL to Hybrid eVTOL

Table 9 shows the same comparison between the three aircraft as in the all-electric section; maximizing payload for a constant 6000 lbs MTOW and 150 kts cruise speed. To take advantage of the hybrid capability, a range of 300 nmi with 45 minute reserves at cruise speed (413 nmi total for the 150 kts) was specified instead. The comparison between the vehicles is similar, between 1.8x and 2.6x payload increase depending on the configuration.

One interesting outcome is that the tilt-rotor does comparatively better than the tilt-duct in the hybrid case. This is due to the fact that the fraction of vehicle weight driven by cruise energy consumption is smaller, so the high cruise efficiency of the tilt-duct is less effective at offsetting the impact of the high propulsion system weight fraction. Since in the hybrid case the batteries are sized by discharge rate, there is a further benefit to the lower peak powers of the tilt-rotor configuration.

	Tilt-Duct eVTOL	Tilt-Rotor eVTOL	eSTOL
MTOW (lb)	6000	6000	6000
Payload (lb)	**767**	**1116**	**1963**
Usable Range (nmi)	300	300	300
Fuel (lb)	438	553	539
Battery (lb)	710	433	226
Installed Motor Power (kW)	1,886	1,769	576
Turbine Power (kW)	216	266	260
Cruise L/D	14.8	10.3	10.5
$f_{batt,TO}$	0.87	0.75	0.62
Cruise Alt. (ft MSL)	5,000	5,000	10,000

Table 9 Comparison of hybrid eVTOL and eSTOL aircraft with a constant 6000 lb MTOW, 300 nmi range, and 150 kts cruise speed.

Another difference between the hybrid and all-electric cases is the eSTOL cruise altitude. In the all-electric case all vehicles cruised at the same minimum allowable cruise altitude, 5000ft, in order to reduce the total energy used. However, in the hybrid case it is optimal for the eSTOL to fly to the highest allowable altitude, which gives higher cruise efficiency as the wing is operating at a higher C_L. Since there is more freedom with the eVTOL configurations to change

wing size there is no cruise efficiency benefit to the higher altitudes; 5000ft is optimal because it minimizes fuel burned in climb. In the engine model used here, specific fuel consumption is assumed to be unchanged with altitude.

It is interesting that the tilt-duct configuration has the lowest fuel burn; again, this is due to the high cruise efficiency of this configuration. The energy required to recharge the battery from the takeoff is included in the fuel burn, but because of the assumed short duration of the takeoff and transition maneuver this does not significantly increase the fuel consumption. Energy to recharge after landing is not included; in some austere locations this may come from the turbine. Fuel burned per pound of payload over an equivalent mission may be the more relevant metric. By that metric, an eSTOL aircraft could carry 1.8x the payload per pound of fuel consumed compared to the tilt-rotor, and 2.1x compared to the tilt-duct. By that metric, the difference between the two eVTOL configurations is smaller.

To this point the vehicle configurations have been compared on the basis of capability for a fixed weight. An alternative approach is to compare configurations based on the vehicle size (defined by maximum takeoff weight) required to fly a given mission. This comparison is sensitive to the maximum span chosen, as shown in Figure 6. The blue line represents the hybrid eSTOL aircraft and the solid and dashed black lines represent the tilt-rotor and tilt-duct configurations, respectively. This color scheme will be used in subsequent plots. For the eVTOL aircraft, since span and

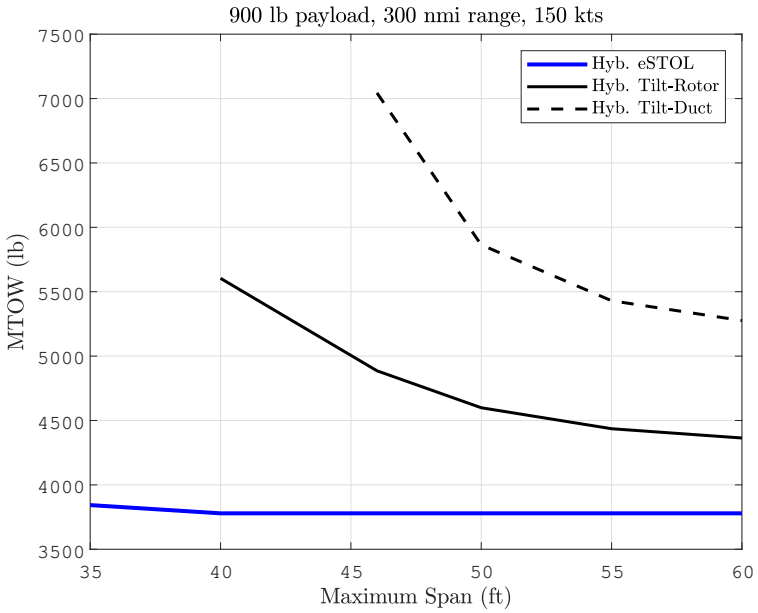

Fig. 6 Sensitivity of eSTOL-eVTOL comparison to span constraint for hybrid-electric configurations

rotor diameter are tied together reducing the span will increase the disk loading, requiring more power and a heavier propulsion system. It is also interesting that at 46 ft. the span constraint is not active for the eSTOL aircraft. This may be an artifact of the choice of objective function - increasing span has a relatively large impact of the wing weight per the model being used, and a relatively small effect on cruise L/D since the induced drag is a small fraction of cruise drag. All-electric configurations (where energy is relatively heavy) favor the more efficient high aspect ratio wing.

Per the relatively simple models used here, increasing eVTOL disk loading will always reduce the total weight, as increases in prop weight, control torque, impacts on cruise efficiency, and other second-order effects which may provide additional upper bounds on prop diameter are not captured. For the comparisons that follow, 50 ft will be used to avoid being in the region of highest sensitivity on the tilt-duct configuration. This is a reasonable upper limit on span for access to constrained areas [26].

One key question is how the advantage of eSTOL aircraft changes with the design ground footprint. So far, 150 ft takeoff ground roll and 100 ft landing ground roll have been used for all comparisons. Takeoff is always the sizing case for the propulsion system. Two comparison studies were conducted showing the impact of changing this ground roll, illustrated in Figure 7. In Figure 7a, the takeoff and landing ground rolls were varied and the aircraft resized at each point. The takeoff and landing ground rolls were assumed to be the same for this study. In Figure 7b(b), total distance over a 50 ft obstacle was specified instead of takeoff distance. The landing ground roll and takeoff ground roll were still constrained to be equivalent. The weights of the two eVTOL aircraft are shown by the two black lines. Climb over a 50

ft obstacle is assumed to be included in the 15 sec takeoff hover for the eVTOL aircraft, and so varying ground footprint has no impact on the sizing. This shows that there are diminishing returns to increasingly short eSTOL ground rolls; for

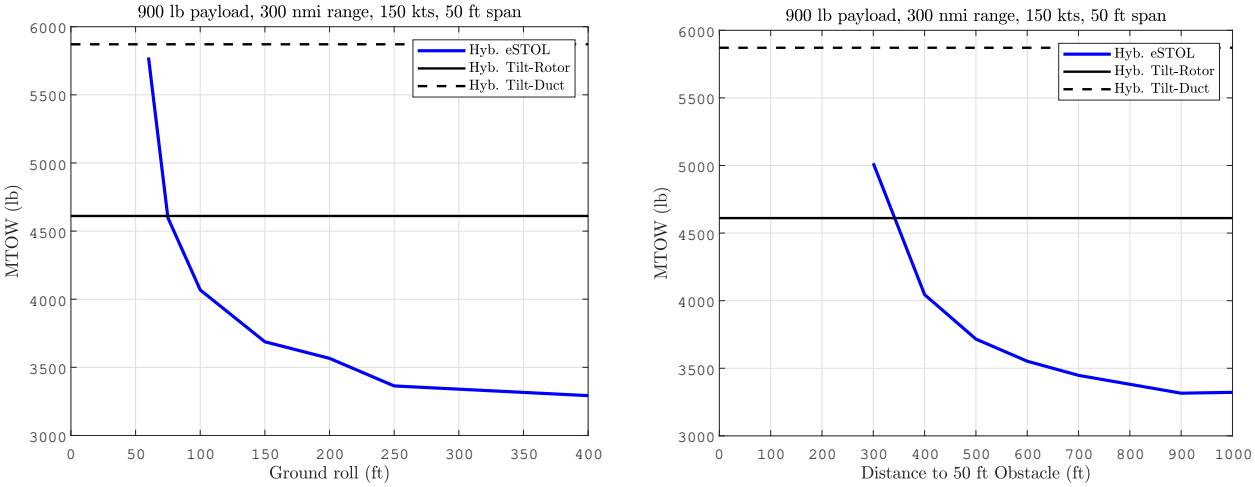

(a) Takeoff ground roll

(b) Total takeoff distance over a 50 ft obstacle

Fig. 7 Impact of changing specified ground roll (a) or total distance over a 50 ft obstacle (b) on eSTOL MTOW for a 900 lb payload, 300 nmi, 150kts design mission.

very short runways the power required for sufficient blown lift and acceleration equals the power required for vertical flight, and there is no performance advantage to eSTOL. This crossover point occurs around 75 ft ground roll or 340ft total takeoff distance. The exact value will vary significantly depending on many of the assumptions about both eSTOL and eVTOL aircraft, as well as the design mission.

However, significant performance advantages can be gained with relatively small increases in ground footprint. It can be seen that 150 ft ground roll is near an inflection point in the curve, making it a good choice for the design point. Figure 8 shows the variation in liftoff C_L of the eSTOL configuration as the ground roll or total takeoff distance is varied. For runways under 100ft the takeoff C_L rapidly increases, and there may be practical limits on achievable C_L especially with takeoff flaps.

Figure 9 shows the impact on the eSTOL and eVTOL comparison of varying the design payload. The difference in MTOW for the three configurations is shown in Figure 9a, and Figure 9b shows the associated variation in wing span (top), installed motor power (middle) and eSTOL takeoff and landing C_L (bottom). This figure shows that eSTOL aircraft scale differently with payload than eVTOL aircraft.

This is an effect of the fixed ground footprint, which constrains the span and rotor size of the eVTOL aircraft. Increasing vehicle weight to accommodate higher payloads increases the disk loading and relative propulsion system weight. While configurations with lower disk loading would shift the eVTOL curves to the right, the trend that the eVTOLs will grow super-linearly with increasing payload would remain unless the span constraint is removed.

In contrast, the eSTOL vehicle scales linearly to higher payloads, even when the span constraint is reached. The weight of the aircraft increases, but because the primary impact is to grow the wing (which is relatively light) the propulsion system weight fractions remain relatively constant. Even when the span constraint is reached, further increase in wing area is possible with a corresponding reduction in aspect ratio and minor reduction in cruise efficiency. This different scaling suggests eSTOL may be an attractive choice for missions where large payload capabilities are desirable. The difference in payload at constant weight used as the comparison basis in previous sections can also be read from this chart, varying from about 1.4x for a 4000lb aircraft to 1.8x for an 8000lb aircraft relative to the tilt-rotor. Comparing the 6000 lb point on this chart (1.6x payload) to Table 9 shows the sensitivity to the assumed disk loading.

Figure 10 shows that, as the mission design speed is varied, there is relatively little impact on the performance differences between eSTOL and eVTOL; increased cruise speed increases the weight of both configurations, although for slightly different reasons. For the eVTOL configurations, as speed increases the wing loading increases in order to keep the vehicle operating at the design C_L. This smaller wing makes the fixed drag areas (fuselage, pylons, etc.) a larger fraction of the total drag, increasing C_{D_0} and reducing the L/D.

The L/D also decreases with increasing speed for the eSTOL configuration, for slightly different reasons. Because

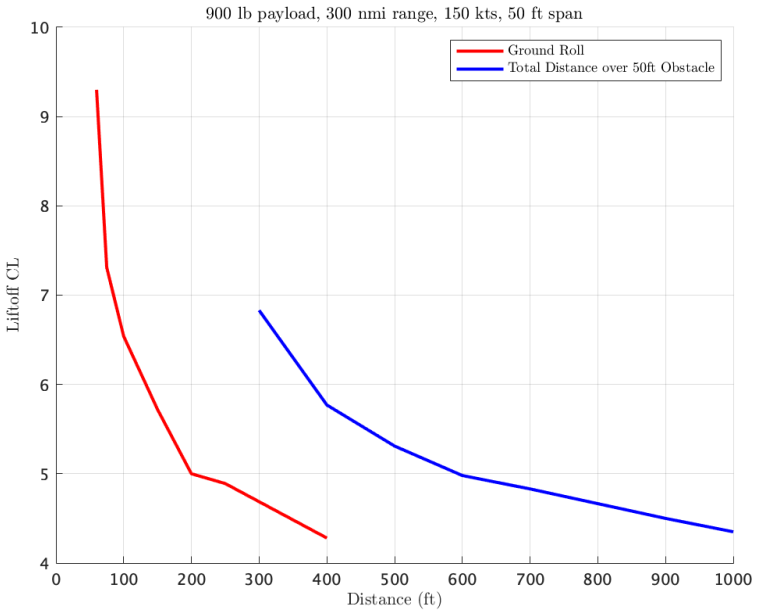

Fig. 8 Variation in liftoff CL with changing ground roll and total takeoff distance to 50 ft obstacle

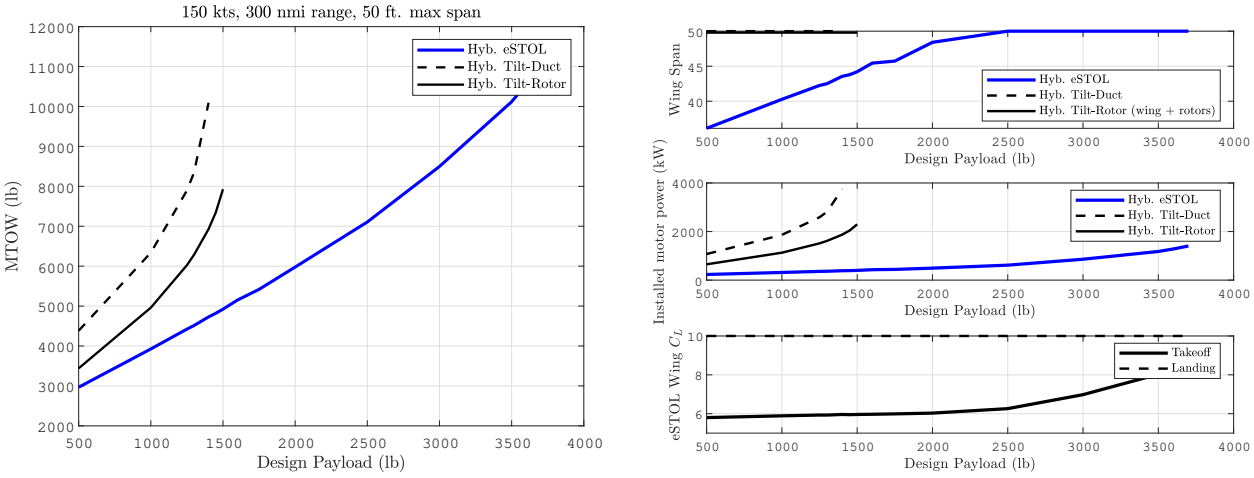

(a) Variation in design payload

(b) Wing span, installed power, and eSTOL C_L

Fig. 9 Impact of varying design payload on eSTOL and eVTOL MTOW (a) and associated variation of key parameters (b)

low wing loading is needed for short takeoff and landing performance, the wing loading can't be adjusted to compensate for the increasing cruise speed (as design takeoff and landing distance is unchanged). Therefore, at higher speeds the wing operates at reduced C_L, reducing efficiency. These competing pressures on wing loading mean that, all else being equal, runway distance and speed will trade with each other for eSTOL aircraft.

Finally, Figure 11 shows how varying the design range affects the comparison. In general, increasing the range is similar to increasing the payload; all aircraft increase in weight, but the eSTOL more slowly than the eVTOL configurations. The difference is less pronounced than with the payload because the higher cruise efficiency of the eVTOL configurations partially offsets the increased disk loading.

There are many more possible missions that may be of interest, and so this is not a comprehensive comparison of the two configurations. Additional fidelity in estimating actuation and propulsion system weights, eVTOL propulsion

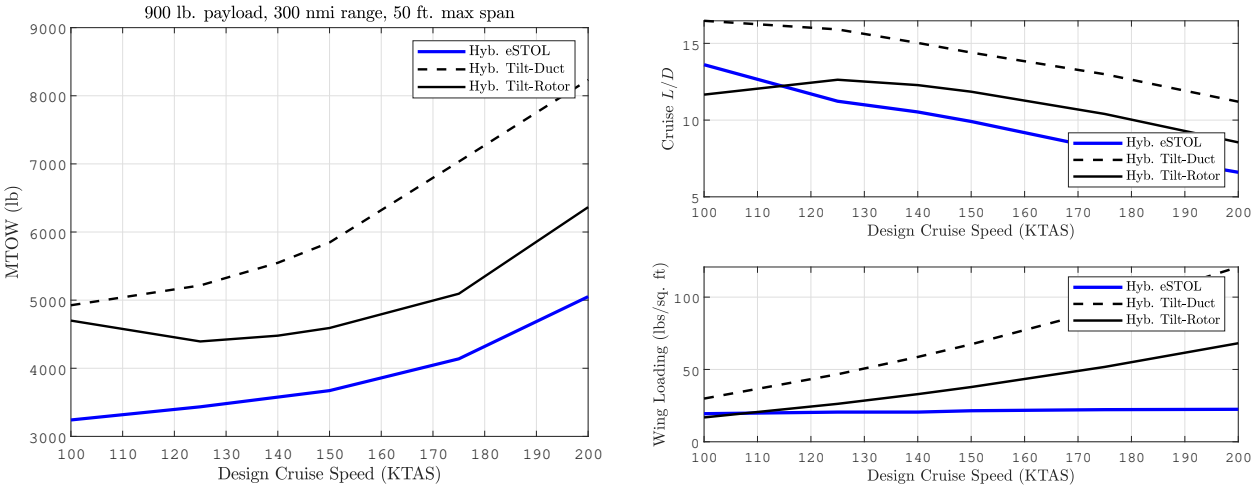

(a) Variation in design cruise speed

(b) Cruise L/D and wing loading

Fig. 10 Impact of varying design payload on eSTOL and eVTOL MTOW (a) and associated variation of key parameters (b)

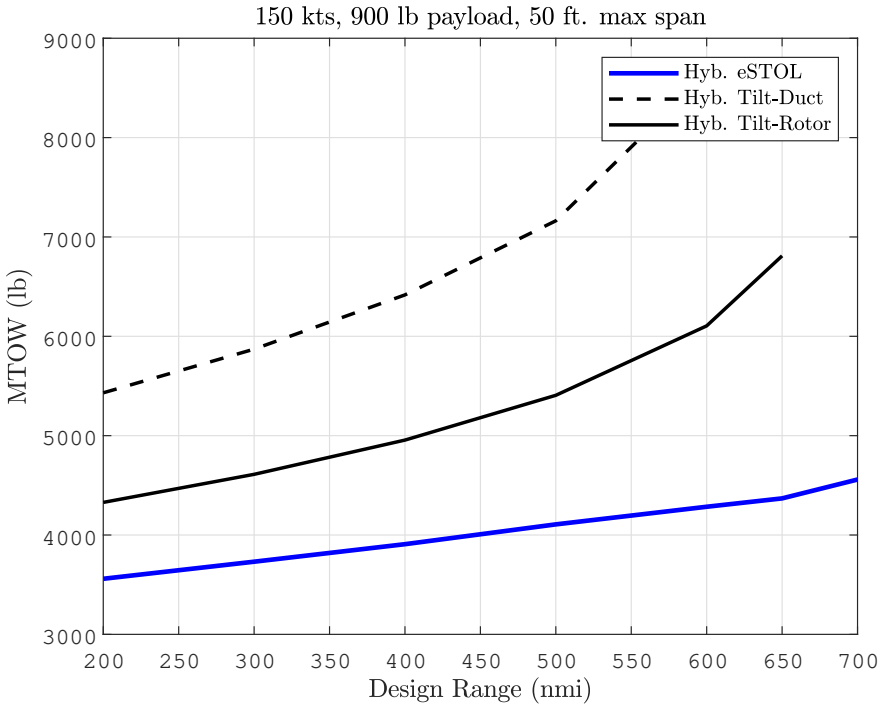

Fig. 11 Change in MTOW with varying design range

system requirements, and how flight control sizes the propulsion system for eSTOL and eVTOL aircraft is required and should be addressed in subsequent efforts.

VII. Conclusion

This work presented on a comparison of eVTOL and eSTOL aircraft optimized for the same mission, with comparable underlying physical assumptions and levels of technology, for both battery-electric and hybrid-electric powertrains. The models were compared against published data for conventional STOL aircraft and proposed eVTOL configurations.

With a design takeoff ground roll of 150 ft, landing ground roll of 100 ft, and a span constraint of 46 ft comparable to proposed eVTOL configurations, a battery-electric eSTOL aircraft can carry 1.9-2.2x the payload of an eVTOL aircraft for the same MTOW, range, and speed, depending on whether the eVTOL is a tilt-rotor or a tilt-duct.

Hybrid powertrains are shown to have performance advantages over all-electric powertrains. A hybrid-electric eSTOL aircraft can carry an equivalent payload 10x further at the same speed and altitude than an all-electric eSTOL of the same MTOW.

Switching from electric propulsion doesn't change the comparison between eSTOL and tilt-rotor eVTOL aircraft significantly; a hybrid eSTOL has a 1.8x increase in payload capability over a hybrid eVTOL, compared to 1.9x in the battery case. The benefit relative to the tilt-duct configuration grows because the benefit of the high cruise L/D is less significant, since stored energy is much lighter.

The comparison between eSTOL and eVTOL is sensitive to the assumed disk loading of the vehicles, which is related to the span constraint in this analysis. At lower disk loadings eVTOL aircraft perform relatively better, but all the trades which impact the selection of the propeller diameter are not captured.

The performance benefits of eSTOL aircraft depend on how short of a runway is required. As ground footprint is decreased and required propulsion system size grows, the performance of eSTOL and eVTOL aircraft becomes similar. In this analysis the crossover point is somewhere between 50-75ft.

The performance benefits of eSTOL aircraft increase as design payload increases, and to a lesser extent range. Increasing speed impacts eSTOL and eVTOL aircraft roughly equally; decreasing speed slightly favors eSTOL aircraft.

This analysis depends on various modeling assumptions which may not be entirely representative of designs being developed. To reduce the uncertainty in this analysis further development of the underlying models is required, especially of eSTOL blown wing performance and eVTOL hover and transition power requirements and associated propulsion system weights.

There are several challenges associated with eSTOL operations, including gust rejection on approach and precision landings, achieving robust control and acceptable handling qualities in low-speed flight, and generating sufficient drag for steep and slow approaches over a 50 ft obstacle. All of these factors will influence the relationship between the takeoff and landing distances quoted in this paper and the size of the actual runway, barge, rooftop or patch of road required.

Blown lift has been implemented on larger aircraft but more work remains to prove that it can be practical and effective at regional aircraft scales and on extremely short runways. This analysis shows that there may be a compelling benefit to the technology, especially for missions which require large payloads, relatively long ranges, and operations outside of existing airport infrastructure.

References

[1] Antcliff, K. et. al., "Regional Air Mobility: Leveraging Our National Investments to Energize the American Travel Experience," 2021. URL https://ntrs.nasa.gov/citations/20210014033.

[2] Uber, "Fast-Forwarding to a Future of On Demand Urban Air Transportation," 2016. URL https://www.uber.com/elevate.pdf, from https://www.uber.com/elevate.pdf. Accessed Oct. 2017.

[3] Christopher B. Courtin, R. J. H., and Drela, M., "Flight Test Results of a Subscale Super-STOL Aircraft," *AIAA 2020 Scitech Forum*, American Institute of Aeronautics and Astronautics, Reston, Virginia, 2020.

[4] Christopher B. Courtin, "An Assessment of Electric STOL Aircraft," Ph.D. thesis, Massachusetts Institute of Technology, Sept 2019.

[5] Courtin, C., Burton, M. J., Yu, A., Butler, P., Vascik, P. D., and Hansman, R. J., *Feasibility Study of Short Takeoff and Landing Urban Air Mobility Vehicles using Geometric Programming*, 2018. https://doi.org/10.2514/6.2018-4151, URL https://arc.aiaa.org/doi/abs/10.2514/6.2018-4151.

[6] Somers, L. A., Justin, C. Y., and Mavris, D. N., "Wind and Obstacles Impact on Airpark Placement for STOL-based Sub-Urban Air Mobility," *AIAA Aviation 2019 Forum*, American Institute of Aeronautics and Astronautics, Reston, Virginia, 2019. https://doi.org/10.2514/6.2019-3121, URL https://arc.aiaa.org/doi/10.2514/6.2019-3121.

[7] Harish, A., Perron, C., Bavaro, D., Ahuja, J., Ozcan, M., Justin, C. Y., Briceno, S. I., German, B. J., and Mavris, D., "Economics of Advanced Thin-Haul Concepts and Operations," *16th AIAA Aviation Technology, Integration, and Operations Conference*, American Institute of Aeronautics and Astronautics, Reston, Virginia, 2016. https://doi.org/10.2514/6.2016-3767, URL http://arc.aiaa.org/doi/10.2514/6.2016-3767.

[8] Spence, D., "The lift coefficient of a thin, jet-flapped wing," *Proceedings of the Royal Society A: Mathematical, Physical and Engineering Sciences*, Vol. 238, 1956. https://doi.org/10.1098/rspa.1956.0203, URL http://rspa.royalsocietypublishing.org/cgi/doi/10.1098/rspa.1959.0116.

[9] Agrawal, D., Asad, F., Berk, B. M., Long, T., Lubin, J., Courtin, C., Drela, M., Hansman, R. J., and Thomas, J. L., "Wind Tunnel Testing of a Blown Flap Wing," *AIAA Aviation 2019 Forum*, American Institute of Aeronautics and Astronautics, Reston, Virginia, 2019. https://doi.org/10.2514/6.2019-3170, URL https://arc.aiaa.org/doi/10.2514/6.2019-3170.

[10] Page, V. R., Dickinson, S. ., and Deckert, W. H., "Large-scale wind-tunnel tests of a deflected slipstream STOL model with wings of various aspect ratios," *NASA TN D-4448*, 1968. URL https://ntrs.nasa.gov/archive/nasa/casi.ntrs.nasa.gov/19680009302.pdf.

[11] Holzhauser, C. A., Innis, R. C., and Quigley, H. C., "Airworthiness considerations for STOL aircraft," 1970. URL https://ntrs.nasa.gov/search.jsp?R=19700006934{&}hterms=D-5594{&}qs=N{%}3D0{%}26Ntk{%}3DAll{%}26Ntt{%}3DD-5594{%}26Ntx{%}3Dmode{%}2520matchallpartial.

[12] Sharpe, P. D., "AeroSandbox: A Differentiable Framework for Aircraft Design Optimization," , 2021.

[13] Andersson, J. A. E., Gillis, J., Horn, G., Rawlings, J. B., and Diehl, M., "CasADi – A software framework for nonlinear optimization and optimal control," *Mathematical Programming Computation*, Vol. 11, No. 1, 2019, pp. 1–36. https://doi.org/10.1007/s12532-018-0139-4.

[14] Biegler, L., and Wächter, A., "On the implementation of an interior-point filter line-search algorithm for large-scale nonlinear programming," *Math. Program*, Vol. 33, No. 106, 2006, p. 25–57. https://doi.org/10.1016/j.compchemeng.2008.08.006.

[15] Nathen, P., "Architectural performance assessment of an electric vertical take-off and landing (e-VTOL) aircraft based on a ducted vectored thrust concept," 2018. https://doi.org/10.2514/6.2018-0105, URL https://lilium.com/files/redaktion/refresh_feb2021/investors/Lilium_7-Seater_Paper.pdf.

[16] Stoll, A., "Analysis and Full Scale Testing of the Joby S4 Propulsion System," 2015. https://doi.org/10.2514/6.2018-0105, URL https://nari.arc.nasa.gov/sites/default/files/attachments/Stoll-TVFW-Aug2015.pdf.

[17] John D. Anderson, Jr, *Aircraft Performance and Design*, McGraw Hill Education, 1999.

[18] McCormick, B. W., *Aerodynamics of V/STOL Flight*, Academic Press, 1967.

[19] R. Johnstone, N. A., "CONDOR - High Altitude Long Endurance (HALE) Automatically Piloted Vehicle (APV)," *AIAA/AHS/ASEE Aircraft Design, Systems and Operations Conference*, American Institute of Aeronautics and Astronautics, Reston, Virginia, 2016. URL http://arc.aiaa.org/doi/10.2514/6.2016-3767.

[20] MAGicALL, "MagiDrive Datasheet," 2021. URL https://www.magicall.biz/products/integrated-motor-controller-magidrive/.

[21] Raymer, D. P., *Aircraft Design: A Conceptual Approach 6th Edition*, AIAA Education Series, 2018.

[22] Torenbeek, E., *Synthesis of Subsonic Airplane Design*, Delft University Press, 1982.

[23] "Pilatus PC-6 SkydiveLillo JD18032008 (cropped).jpg," , 2008. URL https://en.wikipedia.org/wiki/Pilatus_PC-6_Porter#/media/File:Pilatus_PC-6_SkydiveLillo_JD18032008_(cropped).jpg.

[24] Pilatus Aircraft, "PC 6 Fact Sheet," 2008. URL https://web.archive.org/web/20160329155050/http://www.pilatus-aircraft.com/00-def/main/scripts/ckfinder/userfiles/files/Downloads/Brochures/Pilatus%20Aircraft%20Ltd%20-%20Factsheet%20PC-6.pdf.

[25] Stoll, Alex M., et. al., "Conceptual Design of the Joby S2 Electric VTOL PAV," *14th AIAA Aviation Technology, Integration, and Operations Conference*, Reston, Virginia, ???? https://doi.org/10.2514/6.2015-3188, URL https://www.jobyaviation.com/S2ConceptualDesign(AIAA).pdf.

[26] Uber, "UberAir Vehicle Requirements and Missions," 2021. URL https://s3.amazonaws.com/uber-static/elevate/Summary+Mission+and+Requirements.pdf.

[27] Maskell, E. C., and Spence, D. A., "A Theory of the Jet Flap in Three Dimensions," *Proceedings of the Royal Society A: Mathematical, Physical and Engineering Sciences*, Vol. 251, No. 1266, 1959, pp. 407–425. https://doi.org/10.1098/rspa.1959.0116, URL http://rspa.royalsocietypublishing.org/cgi/doi/10.1098/rspa.1959.0116.

[28] Federal Aviation Administration, "Code of Federal Regulations, Title 14, Chapter I, Subchapter C, Part 23: Airworthiness Standards: Normal Category Airplanes," https://www.ecfr.gov, ???? Accessed: 2018-05-12.

[29] Jan Roskam, *Airplane Design*, DARcorporation, 1985.

[30] ASTM, "Standard Specification for Performance of Aircraft," ASTM F3179-20, ASTM International, West Conshohocken, PA, 2021.

Acknowledgments

This work was conducted in collaboration with Electra.aero and supported by the Air Force Agility Prime STTR program through AFWERX contract FA864921P0066. The authors would like to thank Dr. John Langford, the Electra.aero PI, and Dr. Marty Bradley for their support of the project.

A. eSTOL Modeling

There are two key parameters that define the blown wing performance which are not typically used in other contexts. The first is the jet momentum-excess coefficient ΔC_J, which is defined in (1) and repeated here for convenience.

$$* \Delta C_J = \frac{A_d}{S}\left(\frac{V_J^2}{V^2} - 1\right)\left(\frac{V}{V_J} + 1\right) \tag{14}$$

This parameter quantifies the relative strength of the jet compared to the freestream - the larger it is, the more significant the blowing effects are.

The other significant parameter is the net streamwise force coefficient $C_X = C_D - T_c$. This is just the net thrust or drag on the airplane, but since blown wings are a coupled system detailed thrust or drag accounting is ambiguous.

In order to model the performance of the high lift system, the relationship between C_L, C_X, C_M and ΔC_J, α, and δ_F must be estimated. This is in general a complicated problem, and so for the purposes of forming an initial estimate available wind tunnel data for uniformly blown wings is used, specifically from a 1960s wind tunnel test of an aircraft with four motors and full-span blowing [10], as well as a representative blown wing subscale wind tunnel test [9]. Since the latter is a 2D test, handbook estimates for induced drag based on an elliptical blowing distribution [27] and a 0.90 factor on C_L were applied. These are quite crude, but there is very limited data available on blown wings representative of eSTOL configurations.

Better modeling approaches and additional data are required to capture the effects of changing propeller size, flap chord and span, deflection angle, and blowing distribution on the wing. Consequently, there is uncertainty in how well

this model will predict the performance of a well-design eSTOL aircraft. There is a need for improved methods for modeling blown lift aircraft, especially methods suitable for conceptual and preliminary design.

Figure 13 shows representative data from these two sources. The solid lines are from the NASA test [10], and the points are from the subscale wind tunnel test. The points and lines are colored by ΔC_J. One feature which can be noted is that the relatively small propellers have more lift for a given ΔC_J than the larger propellers.

In order to bring this data into the optimization model, the data from both wind tunnel tests was fit over the unstalled flight regime. Figure 12 shows this model fit to a selection of the data set described in [9] for a 40° flap. Figure 13 shows the same model fit to the 40° flap data from [10]. These data sets differ substantially in the relative size of the jet compared to the wing. The same parameters are used to describe both data sets, and interpolation between the two is done on the basis of the ratio of propeller diameter to flap chord $\frac{D_{\text{prop}}}{c_{\text{flap}}}$. Below the stall angle of attack this model shows good agreement with both data sets for the highly blown cases of most interest. Similar agreement is shown across a range of flap deflections. The advantage of this model is that it is very fast to evaluate, differentiable and captures the main effects of highly blown wings up to stall. While the data is publicly available, some parameters of the fit were calibrated based on data supplied by Electra.aero and so are not published here.

There is currently limited test data and analysis methods available for evaluating the performance of eSTOL aircraft, especially with propeller sizes representative of distributed electric propulsion and/or non-uniform blowing across the span. As additional data and better tools become available, it will allow for increased confidence in the eSTOL performance predictions.

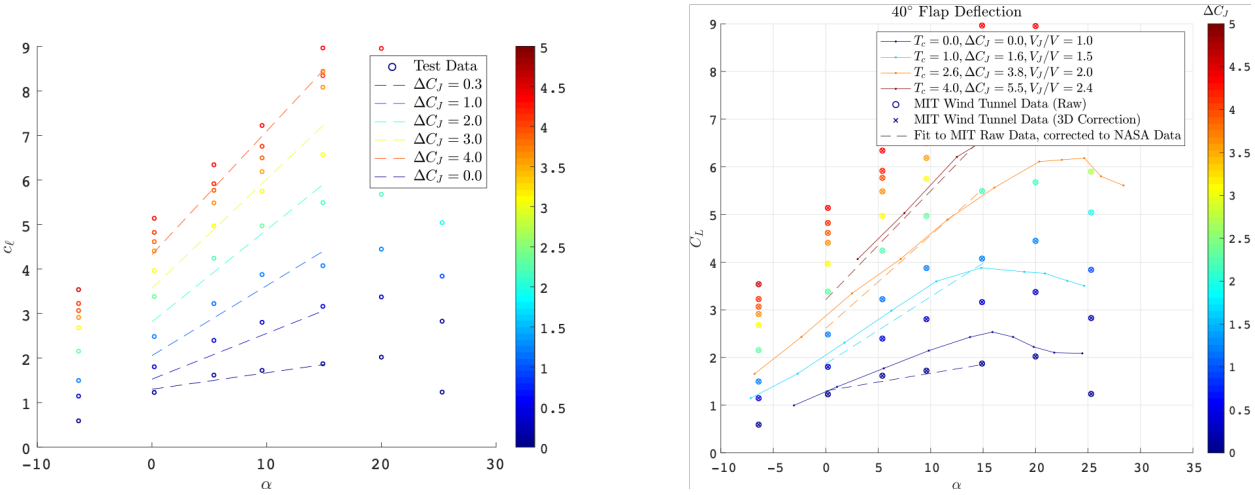

Fig. 13 Modeled predictions (dashed lines) overlaid on subscale test data from [9] (left) and full-scale test data from [10] (right). The subscale test data is also overlaid on the figure at right, showing the benefit of smaller propellers in increasing lift augmentation. Interpolation between the full- and sub-scale data sets is done based on the relative propeller diameter.

A. Takeoff Modeling

Current methods for determining takeoff and landing distance [21] [17] are all predicated on the assumption of a known $C_{L_{\text{max}}}$ in the takeoff and landing conditions. Takeoff and landing speeds can then be known beforehand, based on FAA-defined margins [28] from the stall speed. This makes determining the required takeoff ground roll a straightforward matter of integrating the ground roll equations of motion from zero up to the pre-defined takeoff speed. The landing ground roll is the same process in reverse.

This method does not apply well to eSTOL concepts, where $C_{L_{\text{max}}}$ depends strongly on both installed power and airspeed, and may not be the limiting factor that defines the minimum speed of the aircraft [11]. There is a further issue on landing, in that the usable C_L is limited by the fact that the aircraft must be descending on the approach to landing.

It is necessary, therefore, to take an alternative approach to takeoff and landing calculations which do not require *a priori* assumptions about $C_{L_{\text{max}}}$ but which reflect the real physics which limits eSTOL performance, as well as the the safety margins which are most relevant.

In order to estimate the takeoff distance, the states which define the vehicle trajectory along the takeoff ground roll and obstacle climb are included as free parameters in the vehicle optimization problem, and constrained by the relevant equations of motion - this is a standard trajectory optimization problem. The takeoff is broken up into three phases - brake release to the start of rotation, rotation to liftoff, and liftoff to top of the obstacle.

The longitudinal state **x** and control **u** variables defined along the takeoff trajectory are

$$\mathbf{x} = \begin{bmatrix} s \\ z \\ V \\ \alpha \\ \gamma \\ q \\ C_{L_{\text{Tail}}} \end{bmatrix} \quad \mathbf{u} = \begin{bmatrix} \dot{C_{L_{\text{Tail}}}} \end{bmatrix} \tag{15}$$

Full power is assumed, so it is not included in the control vector. Thrust variation with velocity is calculated via the propeller efficiency model described in Section IV.C. The associated equations of motion during the initial roll are

$$m\dot{V} = -X - \mu(W - L) \tag{16}$$

$$\dot{s} = V \tag{17}$$

$$\dot{\alpha} = 0 \tag{18}$$

$$\dot{q} = 0 \tag{19}$$

with z=0 and γ=0. During rotation, these equations become

$$m\dot{V} = -X - \mu(W - L) \tag{20}$$

$$\dot{s} = V \tag{21}$$

$$\dot{\alpha} = q \tag{22}$$

$$\dot{q} = \frac{M_{\text{MLG}}}{I_{yy}} \tag{23}$$

$$\dot{C_{L_{\text{Tail}}}} = \dot{C_{L_{\text{Tail}_{\text{spec}}}}} \tag{24}$$

again with z=0 and γ=0. The rotation point is defined as the point where pitching moment about the main landing gear equals zero. Pitching moment about the main landing gear is given by

$$M_{\text{MLG}} = M_{\text{wing}} + L_{\text{wing}}\ell_{\text{wing}} - L_{\text{tail}}\ell_{\text{tail}} - W\ell_{\text{cg}} \tag{25}$$

where moments due to acceleration and drag are neglected. It is assumed that the c.g. is at 30% m.a.c., with the landing gear located at 50% mac. Moments of inertia are estimated based on a radius of gyration of 0.34 [29].These numbers will in reality depend significantly on the layout and required c.g. range of the aircraft. Inclusion of the pitching moment is important because of the short duration of eSTOL ground rolls; sufficient rotation capability at low speed may size the tail and/or impact the takeoff distance.

Finally, during the initial climb, the equations are

$$m\dot{V} = -X - W\sin\gamma \tag{26}$$

$$\dot{\gamma} = \frac{g}{V}\left(\frac{L}{W} - \cos\gamma\right) \tag{27}$$

$$\dot{q} = \frac{M_{\text{CG}}}{I_{yy}} \tag{28}$$

$$\dot{z} = V\sin\gamma \tag{29}$$

$$\dot{s} = V \cos\gamma \tag{30}$$

The liftoff point is defined by the satisfaction of the $L = W$ constraint. To ensure an adequate margin from stall, α is limited to $\alpha_{\max} = 10°$. See Section III. In reality, compliance with the existing regulations may also need to be shown based on the implied stall speed, but based on the data available it is expected that this method is more conservative.

Using angle of attack as a reference instead of speed has been suggested in [11] as the basis for safety margins for powered lift aircraft. At the top of the obstacle, $V_{\text{obs}} = 1.1V_{\text{LO}}$. This is based on the typical values of $1.1V_s$ at liftoff[17] and $1.2V_s$ at the top of the obstacle[30].

The models used to calculate L, X, and M as a function of the state and control vectors are described in the following sections. The bounds on the state variables throughout the takeoff roll are

$$5m/s <= V <= 100m/s \tag{31}$$

$$0m <= s <= 3000m \tag{32}$$

$$3° <= \alpha <= 10° \tag{33}$$

$$0°/s <= q <= 20°/s \tag{34}$$

$$-1.5 <= C_{L_{\text{Tail}}} <= 1.5 \tag{35}$$

Finally, flap deflection δ_f is a free parameter bounded by

$$0° <= \delta_f <= 50° \tag{36}$$

The 5 m/s initial condition was chosen to avoid numerical issues with the coefficients becoming very large as airspeed goes to zero. The distance to accelerate from 0 to 5 m/s based on the initial acceleration, assuming no aerodynamic forces apart from thrust, is added to the total ground roll. The takeoff trajectory resulting from the multistage takeoff trajectory optimization problem is given in Figure 14 for an eSTOL vehicle with 500-ft ground footprint.

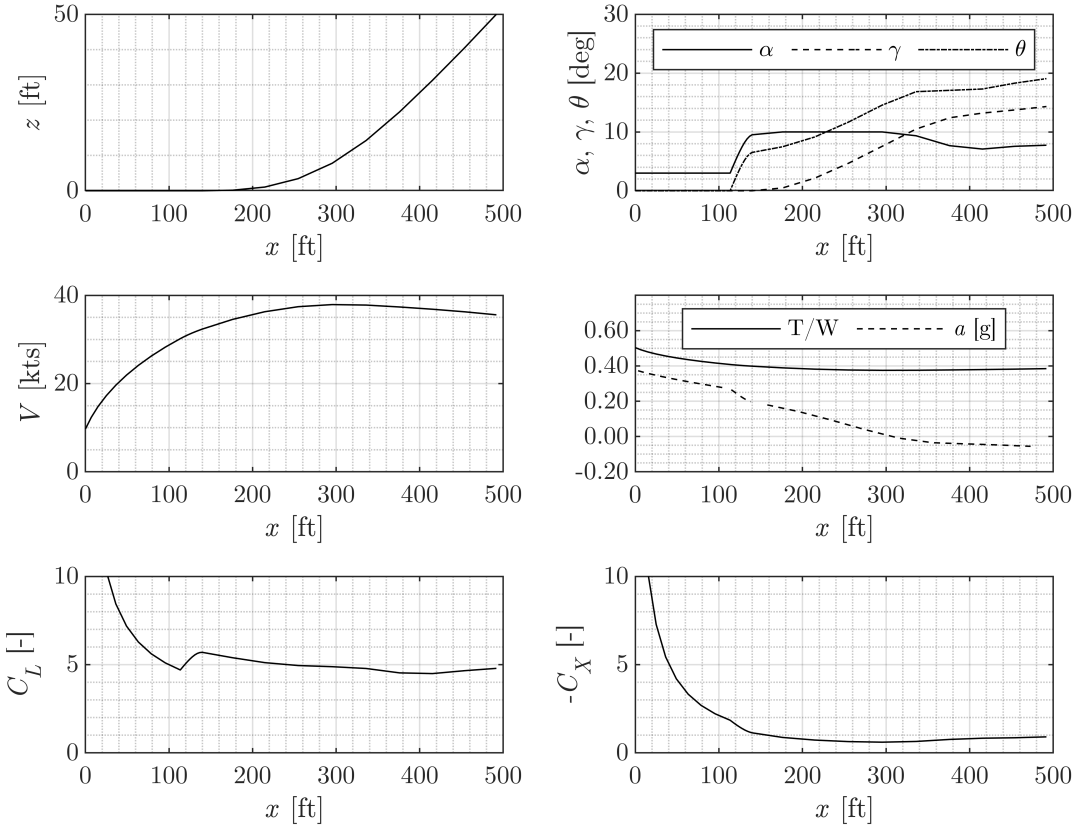

Fig. 14 Optimal takeoff trajectory for an eSTOL vehicle with 500-ft ground footprint

The upper-left plot shows the trajectory of the aircraft; from this it can be seen that liftoff occurs after about 180ft of ground roll. The upper-right plot shows the angle of attack α, flight path angle γ, and pitch angle θ. This shows that rotation is initiated around 120ft, and that maximum angle of attack is a limiting factor. It also shows that continuous adjustment to the pitch attitude is made over the course of the maneuver. In reality, additional constraints may be needed to represent the takeoff procedure given to a pilot (such as holding constant airspeed, angle of attack, or pitch attitude).

Other notable features are the static T/W (about 50% for this particular case, although that will change with design takeoff distance) and the passenger longitudinal acceleration shown in the right middle figure, as well as the continuously varying lift and net streamwise force coefficients from the bottom-left and bottom-right plots. This shows that the accelerations during takeoff are comparable to what might be experienced in automobiles or business jets.

B. eSTOL Landing Distance

The landing ground roll calculation uses the same constraints as the initial takeoff roll. The initial condition is that the vehicle must be in level flight on a -3° flight path at the instant the wheels touch, which corresponds to the end of the flare maneuver. A constant braking friction coefficient of 0.4 is used, and no delay is assumed in brake activation. No reverse thrust is accounted for here although with variable pitch propellers that may offer a path to significantly reduced braking distances. Landing flaps of 70° are assumed. The equations of motion implemented were equations 26 - 30. The second stage modeled the touchdown and landing roll of the airplane along the runway and implemented equations 20 - 24. Bounding equations 31 - 35 were imposed along the landing trajectory. To estimate the energy usage in landing, it is assumed that touchdown power is used for 45 seconds.

B. Detailed Model Outputs

	Tilt-Duct eVTOL	Tilt-Rotor eVTOL	eSTOL
Weight Summary			
MTOW (lb)	6000	6000	6000
Payload (lb)	**668**	**784**	**1474**
Empty Weights (lb)	3596	3356	2754
Battery (lb)	1556	1680	1592
Crew (lb)	180	180	180
Empty Weights			
Structures (lb)	876	881	1213
Lnd. Gear (lb)	210	210	210
Systems, Furnishings, Fixed, Margin (lb)	728	712	685
Propulsion (lb)	1781	1552	647
Propulsion Weights			
Prop or Fan	140	101	34
Motor + Controller	832	780	297
Pwr. Elec.	148	138	53
Motor Install	333	312	119
Wiring	58	45	20
Thermal Management	271	176	124
Key Parameters			
Installed Motor Power (kW)	1,887	1769	672
Shaft Power, Hover (kW)	1,469	954	N/A
Motor Count	36	6	8
Battery Energy (kW-hrs)	177	191	181
Prop or Fan Diameter (ft)	1.0	8.0	4.4
W/S (lbs/sq.ft)	65.5	36.7	25
AR	23.1	8.8	7.9
Span (ft)	46	46 (wing + rotor)	43.7
Mission Performance			
Cruise C_L	1.0	0.56	0.38
Cruise L/D	16.6	11.1	10.5
Cruise Alt. (ft MSL)	5,000	5,000	5,000
Total efficiency in cruise	0.68	0.76	0.76
C_{D_0}	0.0449	0.0381	0.0298
Cruise Energy (kW-hrs)	76	100	110

Table 10 Comparison of battery-only eVTOL and eSTOL aircraft with a constant 6000 lb MTOW, 75 nmi range, and 150 kts cruise speed.

	All-Electric eSTOL	Hybrid eSTOL, Max. Payload	Hybrid eSTOL, Max. Range
Weight Summary			
MTOW (lb)	6000	6000	6000
Payload (lb)	**1474**	**2424**	1474
Empty Weights (lb)	2754	3070	3149
Fuel (lb)	0	97	963
Battery (lb)	1556	225	234
Crew (lb)	180	180	180
Empty Weights			
Structures (lb)	1213	1300	1278
Lnd. Gear (lb)	210	210	210
Systems, Furnishings, Fixed, Margin (lb)	685	719	801
Propulsion (lb)	647	844	856
Propulsion Weights			
Prop	34	30	31
Motor + Controller	297	252	263
Pwr. Elec.	53	45	47
Motor Install	119	101	105
Wiring	20	18	18
Generator	0	71	68
Gearbox	0	29	28
Turbine	0	146	141
Turbine Install	0	44	42
Thermal Management	124	108	113
Key Parameters			
Total Range (nmi)	75	**75**	**747**
Installed Motor Power (kW)	672	572	596
W/S (lb/sq. ft)	25.0	22.2	22.7
Battery Energy (kW-hrs)	180	26	27
Takeoff C_L	6.9	6.4	6.5
V_{LO} (kts)	33	33	32
$f_{batt,TO}$	1.0	0.60	0.63
Landing C_L	8.7	7.7	7.9
V_{TD} (kts)	28	28	28
$f_{batt,LND}$	1.0	0.85	0.86
$f_{batt,climb}$	1.0	0.22	0.24
Cruise altitude	5,000	10,000	10,000
Cruise L/D	10.5	10.6	10.2

Table 11 Comparison of battery-only eSTOL and hybrid eSTOL aircraft with a constant 6000 lb MTOW and 150 kts cruise speed.